

Lateral strain tailoring in manganite homostructures assisted by atomic-flat freestanding membranes

Yufei Wang¹, Yuchen Zhu² (✉), Shengru Chen^{3,4}, Dongke Rong^{3,4}, Qiao Jin^{3,4}, and Er-Jia Guo^{3,4} (✉)

¹ College of Materials Science and Engineering, Beijing University of Chemical Technology, Beijing 100029, China

² State Key Laboratory for Advanced Metals and Materials, University of Science and Technology Beijing, Beijing 100083, China

³ Beijing National Laboratory for Condensed Matter Physics and Institute of Physics, Chinese Academy of Sciences, Beijing 100190, China

⁴ Department of Physics & Center of Materials Science and Optoelectronics Engineering, University of Chinese Academy of Sciences, Beijing 100049, China

© Tsinghua University Press 2023

Received: 19 January 2023 / Revised: 15 February 2023 / Accepted: 24 February 2023

ABSTRACT

Complex oxide thin films exhibit intriguing phenomena due to the coupling between multiple degrees of freedom through interfacial structural engineering. Atomic tailoring of structural parameters determines unique band structure and phonon modes, regulating emergent magnetic and electrical properties of oxide films. However, the construction of different strained and oriented domains in one intact oxide thin film is impossible using conventional means. Here we report the fabrication and quantitative structural analysis of $\text{La}_{0.7}\text{Sr}_{0.3}\text{MnO}_3$ (LSMO) homostructures assisted by atomic-flat freestanding membranes. Pristine substrates and suspended membranes regulate the epitaxial strain and orientation of subsequently grown films. Our results demonstrate an ultrathin transition layer (~ 4 atomic layers) between freestanding membranes and LSMO films is formed due to the strain relaxation. This work offers a simple and scalable methodology for fabricating unprecedented innovative functional oxide homostructures through artificially controlled synthesis routes.

KEYWORDS

transmission electron microscopy, oxide homostructure, freestanding membranes, manganites, strain engineering

1 Introduction

As stated by Nobel Prize Laureate Herbert Kroemer, ‘Often, it may be said that the interface is the device.’ Interface breaks the translational symmetry and generates unique electron system [1–7]. Well-defined interfaces between complex oxide thin films have intriguing physics and fascinating tunable physical properties and are exploited to design transistor, photodetector, solid oxide fuel cells, etc. [8–13]. As a typical perovskite oxide, $\text{La}_{0.7}\text{Sr}_{0.3}\text{MnO}_3$ (LSMO) is a strongly correlated half-metal and classical colossal magnetoresistive material [14, 15]. Furthermore, the physical properties of LSMO strongly depend on oxygen vacancy, film thickness, strain, etc. [8, 9, 15, 16]. For instance, D. A. Muller and coworkers found that the atomic intermixing at the interfaces, and the cation defects in the LSMO degrade the magnetic and transport properties of $\text{La}_{0.7}\text{Sr}_{0.3}\text{MnO}_3/\text{SrTiO}_3$ heterostructure [17]. After these extrinsic defects were eliminated, the room-temperature ferromagnetism was stabilized in five-unit-cell-thick manganite layers. When constructing oxide film heterostructures, the substrates determine the crystallographic orientation, symmetry, and misfit strain of epitaxial thin films grown subsequently. Hence, distinct physical properties of LSMO can be tuned by controlling the interface properties, resulting in tremendous opportunity in magnetic storage applications, magneto-optic, optoelectronic devices, etc. [18–20]. M. Kawasaki and coworkers utilized interface strain and magnetic fields to tune the photocurrent in a p–n junction based on LSMO combined

with semiconducting Nb-doped SrTiO_3 (STO) substrates [21]. By controlling the epitaxial strain, the photocurrent was enhanced threefold under applied magnetic fields.

The precise construction of desired structure in oxide thin films has vital importance in both fundamental research and practical applications. High-quality epitaxial growth provides atomically sharp interfaces. Modified substrate regulates the crystallographic orientation and misfit strain of LSMO thin films. For example, Binghui Ge and coworkers controlled the lattice strain of LSMO thin films through substrate and *in-situ* investigated the strain-dependent topotactic structural transition [12]. Furthermore, in-plane spatial modulations are also one of the most important aspects for fabricating novel oxide interfaces [22, 23]. However, the fabrication of oxide interfaces with variable crystallographic orientations and strain states integrated along a film plane is extremely challenging by conventional layer-by-layer stacking or self-assembling. One possible solution is to artificially modify the single-crystalline substrate [24]. Previously, Wu et al. reported the growth of twisted multiferroic oxides with lateral homostructures [25]. Using acid-soluble manganite layers, they are able to fabricate freestanding membranes and cover the single crystalline substrates. Therefore, the functional oxide films can be rotated in the film plane and stacked with designed twisted angles. Our group had further developed an alternative approach by applying water-soluble sacrificial layers to fabricate ultrathin STO membranes with different orientations [26]. The ferromagnetic

Address correspondence to Yuchen Zhu, zyc930502@outlook.com; Er-Jia Guo, ejguo@iphy.ac.cn

cobaltite films were epitaxially grown on both membranes and substrates strictly following the respective regularity independently, resulting in structural domains with distinct strain states and orientations laterally. Atomically sharp grain boundaries were formed between different structural domains.

Here, we apply the modified substrates to introduce homostructure domains with different strain states into a LSMO single layer. We applied a chemical free and environmental-friendly strategy, in which only the de-ionized water is required to synthesize ≈ 8 -unit-cell-thick freestanding single-crystalline membranes. These membranes were transferred onto the substrate's surface firmly. LSMO thin films were epitaxially grown on both freestanding membranes and substrates, which strictly regulate the strain and orientation of LSMO films. Atomic structures and strain distributions of LSMO thin films were quantitatively analyzed by C_s -corrected Titan G2 transmission electron microscope (TEM) operated at 300 kV. These results demonstrate the successfully construction of structural domains laterally with different strain states and orientations in a single film without breaking the crystallographic symmetry.

2 Results and discussion

The synthesis process of LSMO homostructures was described in Figs. 1(a)–1(e). $Sr_3Al_2O_6$ layer (≈ 30 nm) is a kind of water-soluble material. In order to acquire an ultrathin STO layer (~ 3 nm), they were grown on a (001)-oriented $(LaAlO_3)_{0.3}-(Sr_2AlTaO_6)_{0.7}$ (LSAT) single-crystalline substrate by using pulsed laser deposition (PLD) technique (Fig. 1(a)). Then, the STO layer was attached to a thermal-release tape and delaminated from LSAT substrates after dissolving the sacrificial layer in deionized water (Fig. 1(b)) [27–29]. The freestanding- (FS-) STO membranes maintained their shape and high crystallinity in millimeter size. We paste this small FS-STO membrane on $LaAlO_3$ (LAO) substrates to be a template for subsequent LSMO layer growth (Figs. 1(c) and 1(d)). This allows the subsequent thin LSMO layers to be epitaxially grown on both regions simultaneously. The thickness of LSMO layer grown on these modified substrates is about 40 nm (Fig. 1(e)).

The macroscopic structural characterizations were further performed on LSMO homostructures using conventional X-ray diffraction (XRD). Only (00l) reflections from LSMO films and substrates are observed, demonstrating the high-quality single crystalline film growth, as shown in Fig. 1(f). The pseudo cubic lattice constant of LSMO is 0.386 nm [30], while the lattice

constant of LAO is 0.379 nm. Thus, the LSMO films suffer an in-plane compressive strain of -1.81% from LAO substrates, yielding to an out-of-plane lattice constant of 0.393 nm. The FS-STO membranes serve a different template for LSMO film growth. When released from original substrates, the FS-STO membranes release the misfit strain from the original LSAT substrates. The LSMO films grown on FS-STO membranes exhibit a different strain state compared to LSMO films grown on LAO substrates. Apparently, the LSMO peaks from entire LSMO homostructures shift to a large diffraction angle, indicating a smaller lattice spacing of LSMO films.

In order to precisely characterize the strain distribution in LSMO homostructures, we performed the reciprocal space mapping (RSM) around substrate's (002) reflection. As shown in Fig. 1(g), there are three main reflections in RSM. The strongest reflection is the (002) lattice plane of LAO substrate. The other two reflections are (002) planes of LSMO grown on LAO and FS-STO, respectively. The peak intensity of (002) planes of LSMO grown on LAO is larger than that of LSMO grown on FS-STO due to the larger portion of LSMO films on LAO directly. Simultaneously, we plot the line profiles of RSM in both LSMO/LAO (cut 1) and LSMO/FS-STO/LAO (cut 2) regions. Cut 2 illustrates two peaks at 45.7° and 47.0° , corresponding to the (002) reflections of LSMO films grow on both LAO and FS-STO, respectively. A tiny misalignment of FS-STO membranes during sample transferring was inevitable. Therefore, the diffraction peaks from LSMO/LAO and LSMO/STO are not perfectly aligned at the same q_x . The LSMO grown on FS-STO has a smaller out-of-plane lattice constant (~ 0.386 nm), whereas the LSMO grown on LAO has a relatively larger out-of-plane lattice constant (~ 0.393 nm). These results clearly suggest that the LSMO films exhibit completely different strain states when they are grown on LAO substrate and STO membrane separately.

We further investigate the atomic structures of LSMO homostructures using C_s -corrected TEM. Figure 2(a) is a high-angle annular dark field (HAADF) image of as-prepared LSMO film grown at the terrace of FS-STO. Since the atomic number (Z) of Al is smaller than Sr and Mn, darker contrast at the bottom of the image comes from the LAO substrate and brighter contrast at the upper part of the image is LSMO. At the interface between LAO and LSMO, additional contrast comes from FS-STO. Then, we used energy dispersive spectroscopy (EDS) to analyse the elemental distribution in the black frame. Figure 2(b) shows the corresponding EDS results of the representative region. The signals of Sr and Mn elements indicate the position of LSMO

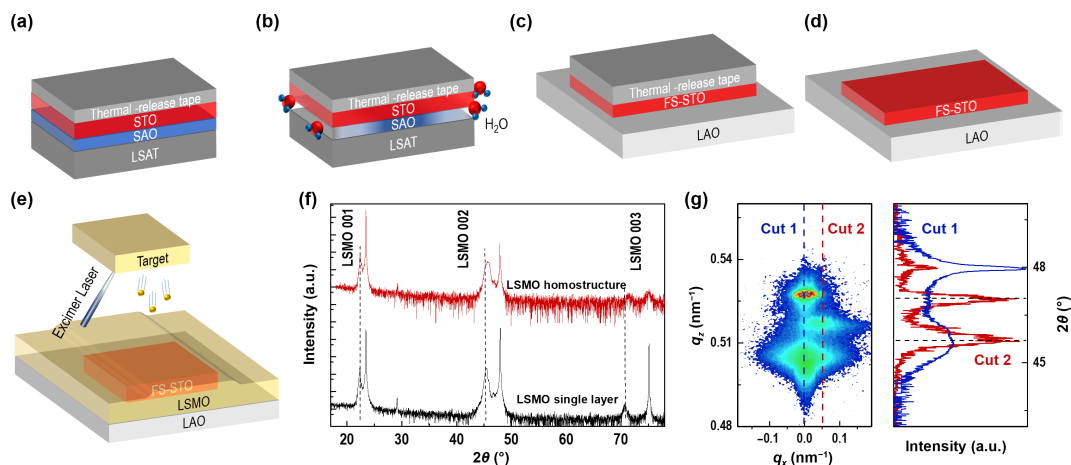


Figure 1 Synthesis of LSMO homostructures. (a)–(e) Schematic of preparation of LSMO homostructures. (f) XRD θ - 2θ scans of LSMO homostructures. Black line is the XRD spectrum collected from LSMO/LAO region, whereas the red line is XRD spectrum collected from LSMO/FS-STO/LAO region. (g) RSM of a LSMO homostructure grown on LAO around substrate's (002) reflection. The (002) reflections of LSMO homostructures split owing to the different strain domains. Inset shows the line profile of cut 1 (blue dashed line) and cut 2 (red dashed line) in RSM.

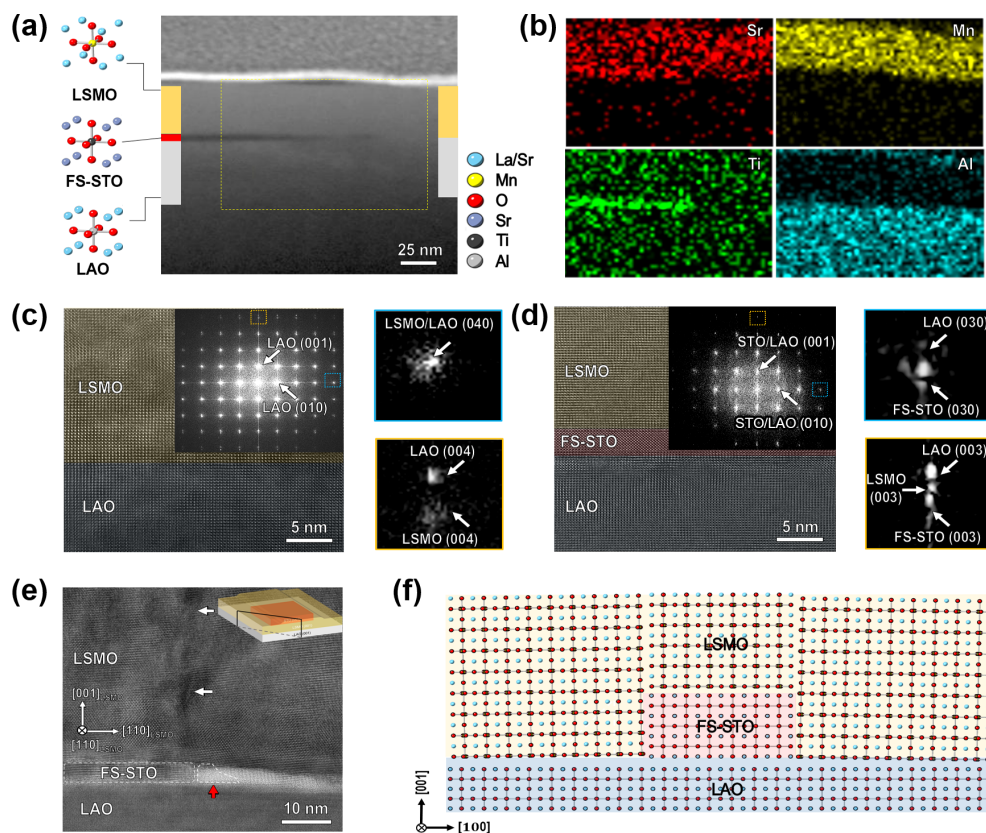


Figure 2 Microscopic structural characterizations of LSMO homostructures. (a) Low-magnified HAADF image of as prepared LSMO homostructures on LAO substrates. Insets show the sample structures and their corresponding atomic models. (b) EDS results from a black frame region in (f). (c) and (d) High-resolution TEM images of a LSMO/LAO heterostructure and a LSMO/FS-STO/LAO heterostructure, respectively. Inset shows the corresponding diffraction patterns. The enlarged diffraction patterns are shown on their right side. (e) TEM image from the domain boundary region. The black frame in the inset indicates the position of the image plane in the sample. Dislocations and structural defects are pointed by white arrows. The red arrow represents the void region. (f) Atomic model of LSMO homostructure grown on FS-STO modified LAO substrates. To simplify the structural model, only 2-unit-cells of FS-STO were illustrated.

layers. Also, we could identify the LAO and FS-STO from EDS signals of Al and Ti, respectively. The bright and uniform contrast from HAADF image and EDS results indicates that the structures of LSMO films grown on FS-STO and LAO are continuous and uniform, and no apparent defects were found in LSMO homostructures. The interfaces between LSMO films and LAO substrates are atomically sharp. However, these interfaces are discontinuous. The right part illustrates that the LSMO layers are grown directly on LAO, while the left part indicates the FS-STO membranes are inserted between LSMO and LAO. The TEM results visualize the presence of FS-STO between LSMO and LAO, demonstrating the successful construction of LSMO homostructures using atomic-flat membranes without breaking its symmetry.

High-resolution TEM (HRTEM) investigations were carried out to provide quantitative analysis of strain distribution within LSMO homostructures. Figure 2(c) shows a representative HRTEM image of LSMO grown on LAO. The HRTEM image is pseudo-coloring, yellow contrast is LSMO, and blue contrast is LAO. We observe an atomically sharp interface between LSMO and LAO. The LSMO layers are coherently grown on LAO, confirming the good epitaxial growth relationship between LSMO and LAO. The contrast of LSMO is bright and uniform, indicating the excellent crystallinity of LSMO. Inset shows the selected area electron diffraction (SAED) pattern of a LSMO/LAO heterostructure. There is only one set of distinct diffraction can be observed, which shows cubic symmetry. Inset with blue frame is enlarged from a representative LAO (040) diffraction spot. Only one distinct diffraction spot is observed, implying that the in-plane lattice constant of LSMO is identical with that of LAO, along with the in-plane direction (LSMO $[0k0]$ // LAO $[0k0]$, LSMO $(h00)$ //

LAO $(h00)$). LSMO thin film has perfect epitaxial relationship with LAO substrate. Inset with yellow frame shows an enlarged view of LAO (004) diffraction spot. The LAO (004) and LSMO (004) diffraction spots are clearly distinguished. According to the diffraction pattern, the spacing of LSMO (004) is ~ 0.098 nm, a bit ($\sim 1.6\%$) larger than the theoretical value of LSMO bulk.

Pseudo-coloring HRTEM image of LSMO/FS-STO/LAO heterostructure is shown in Fig. 2(d). The dark red contrast represents the FS-STO. The interface between LSMO and FS-STO is atomically sharp. The contrast of LSMO is bright and uniform, indicating that the LSMO film grown on STO membrane also has excellent crystallinity. Inset shows a SAED pattern of the LSMO/FS-STO/LAO heterostructure. The diffraction pattern demonstrates a cubic symmetry. Inset with blue frame is enlarged from SAED pattern. We observe two diffraction spots: One is FS-STO (030) lattice plane (spacing 0.129 nm), and another is LAO (030) lattice plane (spacing 0.126 nm). The diffraction spot of LSMO (030) lattice is not present, indicating a perfect epitaxial relationship along the in-plane direction. In the enlarged SAED pattern (yellow frame), three distinct diffraction spots, corresponding to the lattice spacing of 0.129, 0.127, and 0.125 nm, are attributed to FS-STO, LSMO, and LAO, respectively. Analysis on HRTEM and SAED patterns demonstrates that LSMO films grown on LAO suffer an in-plane compression, whereas the LSMO films grown on FS-STO elongate along the in-plane direction. Figure 2(e) shows HRTEM image from the domain boundary region. A void between LSMO, STO, and LAO at the grain boundary, as indicated by a red arrow, is clearly visible. The LSMO layers close to the void are slightly tilted. At the grain boundary of LSMO, some dislocations and structural defects with apparent color contrast are observed, as indicated by white arrows.

According to the HRTEM image, the atomic model of the LSMO/STO/LAO heterostructure was constructed (Fig. 2(f)). The atomic model illustrates the atomic arrangement on the cross section of the heterostructure along $[010]_{\text{LSMO}}$ orientation. We further confirm that the LSMO grown on FS-STO is shrank, and the LSMO grown on LAO is expanded along the out-of-plane direction. There are $\sim 3\%$ misfit strain formed at the grain boundary of LSMO. The strain relaxation at the grain boundary is the main cause of observed defect formation.

Quantitative analysis on the atomic arrangement of LSMO was employed to reveal the accurate strain distribution. Figure 3(a) is an atomic-resolved HRTEM image of LSMO films grown on LAO. According to the HRTEM simulation (in white frames), the bright spots in HRTEM image are La/Sr atoms in LSMO and LAO, and the dark spots are Mn atom in LSMO and Al atom in LAO. Atomic arrangement and lattice relaxation of the nanocrystal were analyzed quantitatively by StatSTEM [31]. Using the pinpoint positions of atom columns by fitting the model function to the intensity maxima of the C_s corrected HRTEM images, a precision of several picometers for the atomic structural details can be achieved [32–34]. The LSMO atomic layers, in parallel to the interface, were labelled as layers 1, 2, etc., from the interface to the surface. The average atomic distance in layer n was labeled as d_n . The average atomic d spacing (d_n) of LSMO films was quantitatively analyzed (Fig. 3(b)). The atomic distance in LSMO films were found to be ~ 379 pm, which is identical to the theoretical lattice constant of LAO, in agreement with our XRD and SAED results. Layer-resolved structural relaxation of LSMO films along the out-of-plane direction was analyzed. The d spacings between atomic layers n and $n + 1$ were labeled as D_n . The layer-resolved D spacing (D_n) of LSMO films were plotted in Fig. 3(c). Consistent with XRD and SAED analysis results, an obvious tensile strain along the out-of-plane direction was found

in LSMO thin films. However, the line chart of layer spacing indicates that the strain was not uniformly distributed along the out-of-plane direction. The layer spacing D_1 – D_3 is close to theoretical value, and the spacing of D_4 and subsequent layers is significantly higher than the theoretical value. Without regarding to D_1 – D_3 , the average atomic layer spacing is 388 pm, only $\sim 0.5\%$ larger than the theoretical value. According to the quantitative analysis of in-plane atomic distance and out-of-plane layer spacing, the unit-cell volume of LSMO film grown on LAO substrate is ~ 0.0560 nm³, $\sim 97.4\%$ of the theoretical value. The good agreement of unit-cell volume between our model and the theoretical one suggests the rationality of our structural model.

Structure relaxation of LSMO thin film grown on FS-STO membranes was further investigated. Atomic-resolved HRTEM image of LSMO film grown on FS-STO is illustrated in Fig. 3(d). The contrast of atomic columns is slightly elliptic, indicating an imperfect imaging condition. After a series of HRTEM image simulation at different imaging conditions, including C_s , de-focus, sample thickness and tilt, beam tilt, etc., the HRTEM simulation image that matches well with the experimental results, is shown in the inset of Fig. 3(d), under the imaging condition of $C_s \sim 3$ μm , de-focus ~ 3.8 nm, sample thickness ~ 30 nm, sample tilt 0° around x axis and -1° around y axis, and beam tilt 0° around x axis and -0.11° around y axis. As shown in HRTEM simulation (Fig. 3(d)), the bright and dark spots are Mn and La/Sr atoms, respectively. The dashed line marks out the interface between LSMO and FS-STO. We find that the interfaces are as sharp as those between the LSMO and LAO. Figure 3(e) shows the average atomic d spacing of the LSMO thin film grown on FS-STO. The HRTEM simulation proves that the sample is slightly tilted along y axis, and the atomic columns in the HRTEM image is slightly elongated along x axis, hence, the error bar of d_n in Fig. 3(e) is larger than that in other line charts. The average atomic d spacings

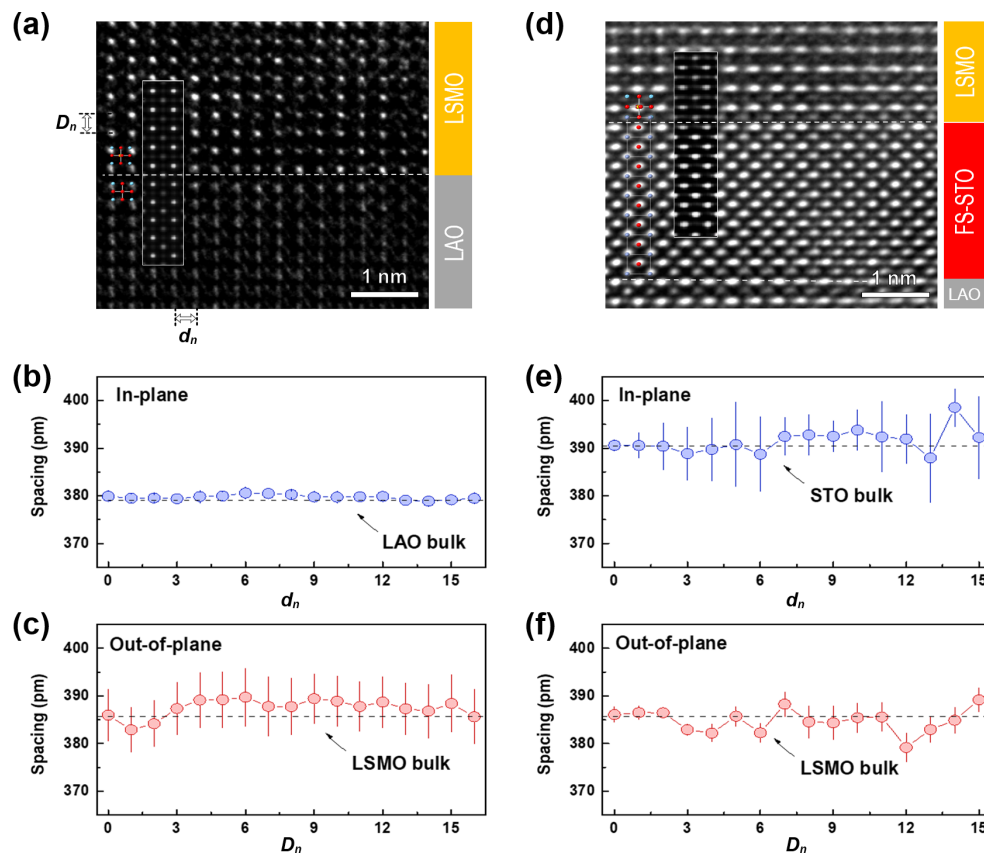


Figure 3 Quantitative analysis of atomic spacing in TEM images. (a) and (d) Atomic-resolved high-resolution TEM images of a LSMO/LAO and a LSMO/FS-STO/LAO heterostructure, respectively. Inset shows the atomic models of each layer. The white frames in (a) and (d) illustrate the simulated TEM images. Line charts of atomic spacing along in-plane ((b) and (e)) and out-of-plane ((c) and (f)) direction in (a) or (d), respectively.

of LSMO films grown on FS-STO were found to be close to that of FS-STO, indicating that LSMO films are uniformly tensile-strained. The average of d_n is 392 pm, $\sim 1.5\%$ larger than the theoretical value. The layer resolved D spacing of the LSMO films on FS-STO is shown in Fig. 3(f). The layer spacing D_1 – D_3 is close to the theoretical value of LSMO lattice constant. Since D_4 layer spacing shifts away from the dashed line. Without considering D_1 – D_3 , the average layer spacing is ~ 384 pm, only $\sim 0.5\%$ smaller than the theoretical value. According to the average d_n and average D_n , the unit-cell volume of a relaxed LSMO film is ~ 0.0587 nm³, $\sim 102.5\%$ of the theoretical value. The quantitative analysis indicates the different lattice strain states present in LSMO films grown on LAO and FS-STO. Furthermore, we note that there is a clear transition layer with a thickness of ~ 4 atomic layers within LSMO films away from the interfaces. The out-of-plane compressive strain reduces to zero after the structural transition. The sharp strain relaxation is surprising because the LSMO is a rather soft material with a tolerant Young's modulus. The volume of relaxed unit-cell for both LSMO films grown on LAO and FS-STO differs from the theoretical value by no more than 3%. The good agreement of unit-cell volume between our model and the theoretical one suggests rationality of our model. These results confirm that out-of-plane lattice distortion is induced by in-plane strain in order to maintain its unit-cell volume.

Previous analysis has proven that the high-quality LSMO thin films can be successfully grown on different substrates. Structural domains with distinct strain states in LSMO thin films form without breaking its symmetry. Actually, the substrate modification present in this work can also be applied to construct homostructures with hybrid crystallographic orientations. Similarly, we tuned the crystallographic orientations of LSMO thin films using identical methodology to study the effect of crystallographic orientation on strain distribution in LSMO thin film. Figure 4(a) shows the schematic diagram of as prepared LSMO hybrid structure. The (001)-oriented FS-STO membrane was attached to the (011)-oriented STO substrate. The area of (001)-STO membranes is designed to be smaller than the (011)-STO substrates to allow subsequent thin LSMO layers to be epitaxially grown on both regions simultaneously. Hence, the LSMO thin film grown on the modified substrate became hybrid structure with two crystallographic orientations. Then, we quantitatively analyzed the lattice parameter of (011)-LSMO films. Figure 4(b) shows XRD θ - 2θ scans of LSMO hybrid structures. Black line is the XRD θ - 2θ scans collected from (011)-LSMO single layer grown on (011)-STO substrates, while the red line is XRD spectrum collected from the entire hybrid structure. Both (00 l) and (0 l l) reflections of LSMO films can be observed from direction patterns. XRD results confirm the excellent epitaxial

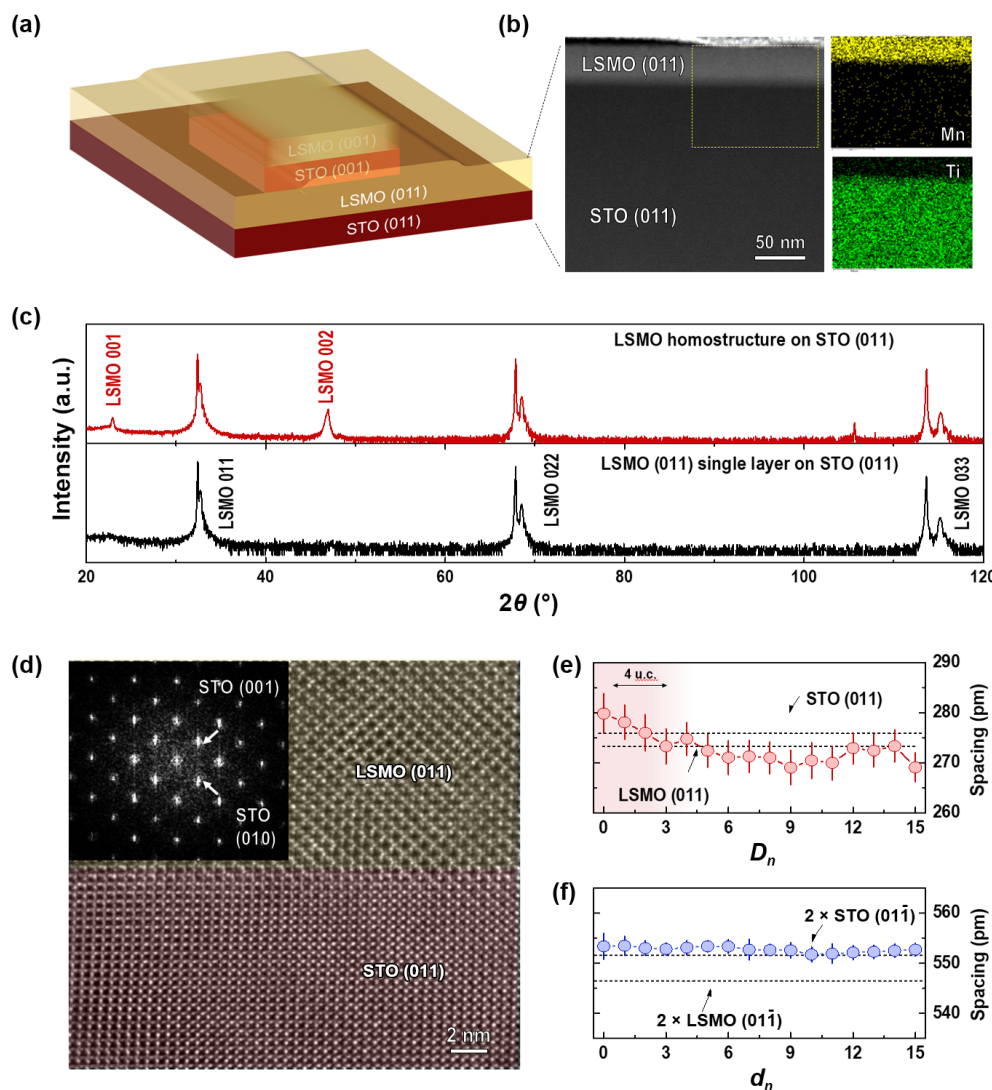


Figure 4 LSMO hybrid structure with different crystallographic orientations. (a) Schematic diagram of sample structure. (b) HAADF image of LSMO grown on (011)-STO substrates and its corresponding EDS mappings. (c) XRD θ - 2θ scans of a LSMO hybrid structure and a LSMO (011) single layer. (d) High-resolution TEM image from the (011)-LSMO/(011)-STO region. Inset shows the corresponding electron diffraction pattern. (e) and (f) Line charts of atomic spacing along the out-of-plane and in-plane direction, respectively.

growth relationship between LSMO films and modified substrates. HAADF image of LSMO film grown on (011)-STO and corresponding EDS mapping are present in Fig. 4(c). The darker contrast represents FS-STO and the brighter contrast represents LSMO. The distribution of Mn signal is identical with the bright contrast region. The uniformed color contrast indicates the excellent crystallinity of LSMO films in both regions. We further show the pseudo-coloring HRTEM image of the (011)-LSMO/(011)-STO region from a hybrid structure in Fig. 4(d). The interface between STO and LSMO is atomically sharp and perfectly coherent. The inset shows the SAED of the (011)-LSMO/(011)-STO region. Only one set of distinct diffraction spots can be easily distinguished, suggesting the perfect epitaxial growth relationship between (011)-LSMO and (011)-STO.

After confirming the high-quality epitaxial growth and crystallinity of (011)-LSMO, quantitative analysis was performed to characterize the strain distribution in (011)-LSMO films. Figure 4(e) is the average atomic d spacing of the LSMO thin film grown on [011] STO substrate. Atomic distances of atomic layers in LSMO films are identical to the theoretical value of STO. Similar to the previous results, there is obvious in-plane strain in (011)-LSMO films. The strained in-plane atomic distance is found to be identical with the (011)-STO substrate, and the average d_n is ~ 553 pm, $\sim 101.3\%$ of the theoretical value of LSMO. The distribution of in-plane atomic distance illustrates the uniform in-plane tensile in the LSMO film. Figure 4(e) is the atomic layer spacing of the LSMO thin film grown on (011)-STO substrates. The value of D_1 – D_3 is obviously larger than the theoretical value. The numerical reduction from D_1 to D_3 is linear. Since D_4 , the atomic layer spacing starts to fluctuate around the theoretical value. In despite of D_1 – D_3 , the average layer spacing D_n is ~ 271 pm, which is slightly smaller than the theoretical value (273 pm, as shown by dashed line), indicating an out-of-plane compressive strain. In consideration of the relaxed in-plane atomic distance and the out-of-plane layer spacing, the unit-cell volume of the (011) LSMO film is ~ 0.0586 nm³, $\sim 101.9\%$ of the theoretical value. These results indicate that the crystallographic orientation and interface lattice mismatch do not affect the strain distribution significantly. In both (001)-LSMO and (011)-LSMO, the strain along in-plane direction is uniformly distributed. A similar structural transition layer with a thickness of ~ 4 atomic layers is observed, indicating the universal out-of-plane strain relaxation process in LSMO films.

3 Conclusions

In summary, we have constructed LSMO homostructures with different strained and crystallographic orientated structural domains. The LSMO homostructures exhibit excellent crystallinity and atomically sharp interface between substrates/membranes underneath. We find that the coherently grown LSMO films are tensile or compressively strained by FS-STO membranes and LAO substrates, respectively. Surprisingly, we observe a clear transition layer with a thickness of ~ 4 atomic layers in both LSMO homostructures, suggesting a rather sharp strain relaxation. These results confirm that the type, density, and location of strain domains are highly controllable using single-crystalline membrane modified substrates. Through accurate strain control, the crystal structure and electron system of LSMO thin film can be delicately tuned, and this method can be applied in construction of other oxide thin film. Our work provides a practical guide and a possible solution for precise construction of oxide homostructures.

4 Experimental section

4.1 Synthesis of LSMO thin film

The water-soluble Sr₃Al₂O₆ (SAO) and STO layers were grown

subsequently on (001)-oriented (LaAlO₃)_{0.3}–(Sr₂AlTaO₆)_{0.7} substrates (Hefei Kejing Mater. Tech. Co., Ltd.) by PLD technique. A focused XeCl excimer laser with duration of ≈ 25 ns, fixed wavelength of 308 nm, and energy density of ~ 1.5 J·cm⁻² was used as the ablation source. The bilayers were deposited at the substrate temperature of 800 °C and oxygen partial pressure of 50 mTorr. The thicknesses of SAO and STO layers were ~ 30 and ~ 3 nm (~ 8 -unit-cells), respectively. On the completion of epitaxy, the STO/SAO bilayers were cooled down to room temperature at the growth pressure. A thermal-release tape (or a polydimethylsiloxane (PDMS), PF-40-X4, Gel-Pak) was pressed firmly on the as-grown sample and then immersed into deionized water at room temperature. After the water-soluble SAO layer was fully dissolved, the ultrathin STO membrane was adhered on the thermal-release tape (or a PDMS). Afterward, the tape-supported STO membranes were transferred on the target substrates, for instance, LaAlO₃ (LAO) substrates, followed by peeling off the thermal-release tape by heating at ~ 90 °C for 10 min. After that, the ultrathin STO membranes remained on the target substrates after detaching the supports. Subsequently, the La_{0.7}Sr_{0.3}MnO₃ thin films with a thickness of ~ 40 nm were fabricated on the prepared substrates by PLD. The thickness of LSMO films was carefully selected by keeping them coherently grown on different target substrates. The LSMO films exhibit distinct physical properties depending on the crystallographic orientation and misfit strain. During the growth of LSMO layers, the substrate temperature was kept at 750 °C and oxygen partial pressure was maintained at 200 mTorr. After the deposition, the samples were cooled down under the oxygen pressure of 100 Torr. The post-oxygen annealing process prevented the formation of oxygen vacancies in the LSMO films, which are well-known to affect their intrinsic physical properties.

4.2 TEM sample preparation

The TEM sample is prepared by focused ion beam (FIB). A slice was cut out from the LSMO/STO/LAO heterostructure along the direction parallel to the out-of-plane direction ((001)-LAO, and (001)-membrane STO for LSMO/(001)-STO/(011)-STO heterostructure) and edge of the film ((010)-LAO, and (010)-membrane STO for LSMO/(001)-STO/(011)-STO heterostructure). In other words, the slices are perpendicular to the [100]-LSMO orientation ([100]-membrane STO for LSMO/(001)-STO/(011)-STO heterostructure). During the TEM observation, the direction of electron beam is the in-plane direction ([100]-LSMO orientation for LSMO/STO/LAO heterostructure, and [100]-membrane STO for LSMO/(001)-STO/(011)-STO heterostructure) of the film.

4.3 Atomic position characterizations

HAADF and HRTEM images of the LSMO thin film were obtained on a Titan G2 system operated at 300 kV. The aberration corrector was used to set the coefficient of spherical aberration to a minimum of $C_s \sim 3$ μm. TEM images were recorded on a Gatan camera. EDS data were collected on an Oxford Max 80T energy dispersive spectroscopy. A fit of 2D Gaussians to the intensity distribution of the atomic columns was used to determine the atomic position from HRTEM images for subsequent analysis [32]. After the determination of atomic coordinate, the atomic distance of each pair of adjacent atoms can be calculated and hence the average atomic distance in each atomic layer can be obtained. Then, linear fitting of each atomic layer based on the atomic coordinate was applied to calculate the slope of these atomic layers. The average slope of these atomic layers reflects the tilt of the HRTEM image. Then, the HRTEM image was tilted to acclinic based on the average slope. After the tilt, the atomic layers

in the HRTEM image can be considered as aclinic. At this case, the average y coordinate of atoms in atomic layer n (y_n) in the tilted image was calculated. Then, the layer spacing between atomic layer n and atomic layer $n + 1$ can be calculated as Eq. (1)

$$|y_n - y_{n+1}| \quad (1)$$

The error bar is calculated as Eq. (2)

$$SE_n = \frac{SD_n}{\sqrt{x}} \quad (2)$$

where SE is standard error, SD_n is the standard deviation of each atomic layer n , and x is the number of atoms in atomic layer n .

Acknowledgements

This work was supported by the National Key Basic Research Program of China (No. 2020YFA0309100), the National Natural Science Foundation of China (Nos. 51971025, 12034002, 11974390, U22A20263, and 52250308), the Beijing Natural Science Foundation (No. 2212034), the Guangdong-Hong Kong-Macao Joint Laboratory for Neutron Scattering Science and Technology (No. HT-CSNS-DG-CD-0080/2021), and the Strategic Priority Research Program (B) of the Chinese Academy of Sciences (No. XDB33030200).

References

- [1] Mannhart, J.; Schlom, D. G. Oxide interfaces—an opportunity for electronics. *Science* **2010**, *327*, 1607–1611.
- [2] Liu, Y.; Huang, Y.; Duan, X. F. Van der Waals integration before and beyond two-dimensional materials. *Nature* **2019**, *567*, 323–333.
- [3] Zhang, Z. C.; Xu, B.; Wang, X. Engineering nanointerfaces for nanocatalysis. *Chem. Soc. Rev.* **2014**, *43*, 7870–7886.
- [4] Cheng, Y. X.; Zhao, S. S.; Zhou, Z. Y.; Liu, M. Recent development of E-field control of interfacial magnetism in multiferroic heterostructures. *Nano Res.*, in press, DOI: 10.1007/s12274-022-5125-5.
- [5] Azadmanjiri, J.; Srivastava, V. K.; Kumar, P.; Wang, J.; Yu, A. M. Graphene-supported 2D transition metal oxide heterostructures. *J. Mater. Chem. A* **2018**, *6*, 13509–13537.
- [6] Cao, Y. D.; Sun, Y. H.; Yang, H. H.; Zhou, L.; Huang, Q. M.; Qi, J. J.; Guan, P. F.; Liu, K. H.; Wang, R. M. Directional migration and rapid coalescence of Au nanoparticles on anisotropic ReS_2 . *Nano Lett.* **2023**, *23*, 1211–1218.
- [7] Zhang, B.; Yun, C.; Wu, H.; Zhao, Z. J.; Zeng, Y.; Liang, D.; Shen, T.; Zhang, J. N.; Huang, X. X.; Song, J. P. et al. Two-dimensional wedge-shaped magnetic EuS : Insight into the substrate step-guided epitaxial synthesis on sapphire. *J. Am. Chem. Soc.* **2022**, *144*, 19758–19769.
- [8] Yadav, A. K.; Nelson, C. T.; Hsu, S. L.; Hong, Z.; Clarkson, J. D.; Schlepütz, C. M.; Damodaran, A. R.; Shafer, P.; Arenholz, E.; Dedon, L. R. et al. Observation of polar vortices in oxide superlattices. *Nature* **2016**, *530*, 198–201.
- [9] Yao, L. D.; Inkinen, S.; Van Dijken, S. Direct observation of oxygen vacancy-driven structural and resistive phase transitions in $\text{La}_{2/3}\text{Sr}_{1/3}\text{MnO}_3$. *Nat. Commun.* **2017**, *8*, 14544.
- [10] Yu, W. J.; Sun, X. R.; Xiao, M.; Hou, T.; Liu, X.; Zheng, B. L.; Yu, H.; Zhang, M.; Huang, Y. L.; Hao, X. J. Recent advances on interface engineering of perovskite solar cells. *Nano Res.* **2022**, *15*, 85–103.
- [11] Huang, J. J.; Wang, H.; Sun, X.; Zhang, X. H.; Wang, H. Y. Multifunctional $\text{La}_{0.67}\text{Sr}_{0.33}\text{MnO}_3$ (LSMO) thin films integrated on mica substrates toward flexible spintronics and electronics. *ACS Appl. Mater. Interfaces* **2018**, *10*, 42698–42705.
- [12] Hu, K. J.; Zhang, X. Y.; Chen, P. F.; Lin, R. J.; Zhu, J. L.; Huang, Z.; Du, H. F.; Song, D. S.; Ge, B. H. Atomic-scale observation of strain-dependent reversible topotactic transition in $\text{La}_{0.7}\text{Sr}_{0.3}\text{MnO}_x$ films under an ultra-high vacuum environment. *Mater. Today Phys.* **2022**, *29*, 100922.
- [13] Yusefi Sarraf, S.; Singh, S.; Garcia-Castro, A. C.; Trappen, R.; Mottaghi, N.; Cabrera, G. B.; Huang, C. Y.; Kumari, S.; Bhandari, G.; Bristow, A. D. et al. Surface recombination in ultra-fast carrier dynamics of perovskite oxide $\text{La}_{0.7}\text{Sr}_{0.3}\text{MnO}_3$ thin films. *ACS Nano* **2019**, *13*, 3457–3465.
- [14] Srinivasan, G.; Rasmussen, E. T.; Levin, B. J.; Hayes, R. Magnetoelectric effects in bilayers and multilayers of magnetostrictive and piezoelectric perovskite oxides. *Phys. Rev. B* **2002**, *65*, 134402.
- [15] Huang, B. C.; Yu, P.; Chu, Y. H.; Chang, C. S.; Ramesh, R.; Dunin-Borkowski, R. E.; Ebert, P.; Chiu, Y. P. Atomically resolved electronic states and correlated magnetic order at termination engineered complex oxide heterointerfaces. *ACS Nano* **2018**, *12*, 1089–1095.
- [16] Biegalski, M. D.; Dörr, K.; Kim, D. H.; Christen, H. M. Applying uniform reversible strain to epitaxial oxide films. *Appl. Phys. Lett.* **2010**, *96*, 151905.
- [17] Mundy, J. A.; Hikita, Y.; Hidaka, T.; Yajima, T.; Higuchi, T.; Hwang, H. Y.; Muller, D. A.; Kourkoutis, L. F. Visualizing the interfacial evolution from charge compensation to metallic screening across the manganite metal-insulator transition. *Nat. Commun.* **2014**, *5*, 3464.
- [18] Navasery, M.; Halim, S. A.; Bahmanrokh, G.; Erfani, H. M.; Soltani, N.; Dehzhangi, A.; Kamalianfar, A.; Din, F. U.; Abdolmohammadi, S.; Chen, S. K. et al. Characterization and conduction mechanism of $\text{La}_{5/8}\text{Sr}_{3/8}\text{MnO}_3$ thin films prepared by pulsed laser deposition on different substrates. *Int. J. Electrochem. Sci.* **2013**, *8*, 6905–6921.
- [19] Tang, X. G.; Liu, Q. X.; Jiang, Y. P.; Zheng, R. K.; Chan, H. L. W. Enhanced dielectric properties of highly (100)-oriented $\text{Ba}(\text{Zr}, \text{Ti})\text{O}_3$ thin films grown on $\text{La}_{0.7}\text{Sr}_{0.3}\text{MnO}_3$ bottom layer. *J. Appl. Phys.* **2006**, *100*, 114105.
- [20] Samet, L.; Imhoff, D.; Maurice, J. L.; Contour, J. P.; Gloter, A.; Manoubi, T.; Fert, A.; Colliex, C. EELS study of interfaces in magnetoresistive LSMO/STO/LSMO tunnel junctions. *Eur. Phys. J. B Condens. Matter Complex Syst.* **2003**, *34*, 179–192.
- [21] Sheng, Z. G.; Nakamura, M.; Koshibae, W.; Makino, T.; Tokura, Y.; Kawasaki, M. Magneto-tunable photocurrent in manganite-based heterojunctions. *Nat. Commun.* **2014**, *5*, 4584.
- [22] Davydenko, A. V.; Kozlov, A. G.; Chebotkevich, L. A. Spatial modulation of in-plane magnetic anisotropy in epitaxial $\text{Co}(111)$ films grown on macrostep-bunched $\text{Si}(111)$. *J. Appl. Phys.* **2014**, *116*, 143901.
- [23] Pandurangi, S. S.; Kulkarni, S. S. Mechanics of wrinkling of a thin film bonded to a compliant substrate under the influence of spatial thermal modulation. *Int. J. Solids Struct.* **2015**, *62*, 124–133.
- [24] Cortie, D. L.; Shueh, C.; Lai, B. C.; Pong, P. W. T.; Lierop, J. V.; Klose, F.; Lin, K. W. The effect of single crystalline substrates and ion-beam bombardment on exchange bias in nanocrystalline $\text{NiO}/\text{Ni}_{80}\text{Fe}_{20}$ bilayers. *IEEE Trans. Magn.* **2014**, *50*, 1–4.
- [25] Wu, P. C.; Wei, C. C.; Zhong, Q. L.; Ho, S. Z.; Liou, Y. D.; Liu, Y. C.; Chiu, C. C.; Tzeng, W. Y.; Chang, K. E.; Chang, Y. W. et al. Twisted oxide lateral homostructures with conjunction tunability. *Nat. Commun.* **2022**, *13*, 2565.
- [26] Chen, S. R.; Zhang, Q. H.; Rong, D. K.; Xu, Y.; Zhang, J. F.; Pei, F. F.; Bai, H.; Shang, Y. X.; Lin, S.; Jin, Q. et al. Braiding lateral morphotropic grain boundaries in homogenetic oxides. *Adv. Mater.* **2023**, *35*, 2206961.
- [27] Lu, D.; Baek, D. J.; Hong, S. S.; Kourkoutis, L. F.; Hikita, Y.; Hwang, H. Y. Synthesis of freestanding single-crystal perovskite films and heterostructures by etching of sacrificial water-soluble layers. *Nat. Mater.* **2016**, *15*, 1255–1260.
- [28] Ji, D. X.; Cai, S. H.; Paudel, T. R.; Sun, H. Y.; Zhang, C. C.; Han, L.; Wei, Y. F.; Zang, Y. P.; Gu, M.; Zhang, Y. et al. Freestanding crystalline oxide perovskites down to the monolayer limit. *Nature* **2019**, *570*, 87–90.
- [29] Dong, G. H.; Li, S. Z.; Yao, M. T.; Zhou, Z. Y.; Zhang, Y. Q.; Han, X.; Luo, Z. L.; Yao, J. X.; Peng, B.; Hu, Z. Q. et al. Super-elastic ferroelectric single-crystal membrane with continuous electric dipole rotation. *Science* **2019**, *366*, 475–479.

- [30] Moon, E. J.; He, Q.; Ghosh, S.; Kirby, B. J.; Pantelides, S. T.; Borisevich, A. Y.; May, S. J. Structural “ δ doping” to control local magnetization in isovalent oxide heterostructures. *Phys. Rev. Lett.* **2017**, *119*, 197204.
- [31] De Backer, A.; Van Den Bos, K. H. W.; Van Den Broek, W.; Sijbers, J.; Van Aert, S. StatSTEM: An efficient approach for accurate and precise model-based quantification of atomic resolution electron microscopy images. *Ultramicroscopy* **2016**, *171*, 104–116.
- [32] Wang, R. M.; Dmitrieva, O.; Farle, M.; Dumpich, G.; Ye, H. Q.; Poppa, H.; Kilaas, R.; Kisielowski, C. Layer resolved structural relaxation at the surface of magnetic FePt icosahedral nanoparticles. *Phys. Rev. Lett.* **2008**, *100*, 017205.
- [33] Zhu, Y. C.; Sun, Y. H.; Zhang, H. Z.; He, Y.; Liu, W.; Wang, R. M. Interface structure and strain controlled Pt nanocrystals grown at side facet of MoS₂ with critical size. *Nano Res.* **2022**, *15*, 8493–8501.
- [34] Zhao, H. F.; Zhu, Y. C.; Ye, H. Y.; He, Y.; Li, H.; Sun, Y. F.; Yang, F.; Wang, R. M. Atomic-scale structure dynamics of nanocrystals revealed by *in-situ* and environmental transmission electron microscopy. *Adv. Mater.*, in press, DOI: 10.1002/adma.202206911.